Supplementary information

Laser-induced synthesis of polyoxometalate-derived Fe_2O_3–MoO_3 heterostructure to boost oxygen evolution reaction

Ting-Ting Liu, [b] Peng Luo, [c] Zixuan Wu, [c] Jun-Rui Chen, [c] Yan Zou, [a] Dongsheng Geng, [a] and Yu-Jia Tang *[a]

[a] School of Chemistry and Materials Science, Nanjing University of Information Science and Technology, 219 Ningliu Road, Nanjing, 210044, P. R. China

[b] School of Teacher Education, Nanjing University of Information Science and Technology, 219 Ningliu Road, Nanjing, 210044, P. R. China

[c] Reading academy, Nanjing University of Information Science and Technology, 219 Ningliu Road, Nanjing, 210044, P. R. China

E-mail: tangyujia@nuist.edu.cn

Experimental

Synthesis of Fe_2O_3–MoO_3 on NF: Fe_2O_3–MoO_3 was synthesized via a two-step method. 0.1 mmol of PMo_{12} and 1 mmol of $Fe(NO_3)_3 \cdot 9H_2O$ with a Mo/Fe molar ratio of 1.2:1 were dissolved in 50 mL of deionized water by ultrasonication. The pH of the above mixture was adjusted to 8 using a 1.0 M KOH solution, forming a PMo_{12} dispersed iron hydroxide precipitate of PMo_{12}–$Fe(OH)_3$. The PMo_{12}–$Fe(OH)_3$ precursor was dispersed in a mixed solution of water/ethaol to form a suspension, and then coated on the NF support with a loading mass of 2 mg cm^{-2}. The laser annealing treatment was proceeded on a laser machine equipped with a CO_2 laser (CX-30s, Chanxan Laser). The laser power and speed were set to be 9 W and 400 mm s^{-1}, respectively, to obtain the Fe_2O_3–MoO_3 heterostructure on NF. Control samples of Fe_2O_3 and MoO_3 on NF were prepared by laser annealing the pH-regulated $Fe(NO_3)_3$ and PMo_{12} precursors, separately.

Physical characterizations: X-ray diffraction (XRD) data were obtained using a Smart Lab/3kW diffractometer with Cu Kα radiation. A Gemini SEM 300 field emission scanning electron microscope (SEM) was applied to observe the surface morphologies. Energy dispersive X-ray (EDX) spectroscopy was acquired by SEM equipped with an X-max Oxford detector. Structrual characterizations were performed using a high-resolution transmission electron microscope (HRTEM, FEI Tecnai G2 F30 S-Twin) at 300 kV. X-ray photoelectron spectroscopy (XPS) tests were performed using an Escalab Xi+ X-ray spectrometer with Al Kα radiation. XPS depth profiling characterizations were performed with Ar^+ sputtering at intervals of 20 s. Etch rate of an Ar^+ ion beam was set to be 0.4 nm s^{-1} and etch energy was 2 kV. Ultraviolet-visible diffuse reflectance spectra (UV-Vis DRS) measurements were performed on a UV-vis spectrophotometer (Shimadzu UV2600i). Raman spectra were obtained from a Laser Microscopic Confocal Raman Spectrometer (LabRam HR800) with a 532 nm laser.

Electrochemical measurements: OER electrocatalytic performances were measured by an electrochemical workstation (CORRTEST CS2350M) with a three-electrode system at room temperature. Fe_2O_3–MoO_3 on NF (1 × 0.5 cm^2), Hg/HgO electrode, and graphite rod were applied as working, reference, and counter electrodes, respectively. Linear scanning voltammetry (LSV) curves were evaluated at a scan rate of 2 mV s^{-1} in 1.0 M KOH electrolyte. The LSV curves were used with 90% *iR* compensation. The uncompensated *iR* correction is calculated using the following equation: $E = E_{\mathrm{RHE}} - iR_{\mathrm{s}}$, where E is the *iR*-corrected potential, E_{RHE} is the measured potential versus reversible hydrogen electrode, i is the measured current, R_{s} is uncompensated solution resistance. Double-layer capacitance (C_{dl}) was calculated by measuring cyclic voltammetry (CV) curves at different scan rates (20−120 mV s^{-1}) within a non-faradic potential range (0−0.1 V vs. Hg/HgO). Electrochemical impedance spectroscopy (EIS) were measured in a frequency range of 100,000 to 0.01 Hz with an amplitude of 10 mV at an overpotential of 300 mV. Long-term stability test was recorded by chronopotentiometry (CP) at a current density of 100 mA cm^{-2} over 120 h. All the potentials were normalized to reversible hydrogen electrode (RHE) scale by adding an value of 0.924 V.

Advantages of laser annealing strategy: Compared with the conventional high-temperature annealing method in a tube furnace, the laser annealing treatment could generate new components with defects via the instantaneous localized high temperature and rapid cooling, thus presenting unique advantages for the synthesis of POM-derived metal oxides as efficient OER electrocatalysts. On the one hand, the high-energy laser annealing can rapidly destroy the crystalline structure, leading the fast decomposition of PMo_{12} and its conversion to metal oxides. The laser treatment could simultaneously generate abundant vacancies and amorphous structures, contributing to the enhanced OER activity. On the other hand, the CO_2 laser has a weak penetration ability, which effectively prevents the severe thermal oxidation of the NF substrate and the agglomeration of nanoparticles. The NF substrate is well maintained, and the active components remain highly dispersed. Thus, the laser annealing reaction facilitates the construction of heterostructures, thereby optimizing the electron transport efficiently.

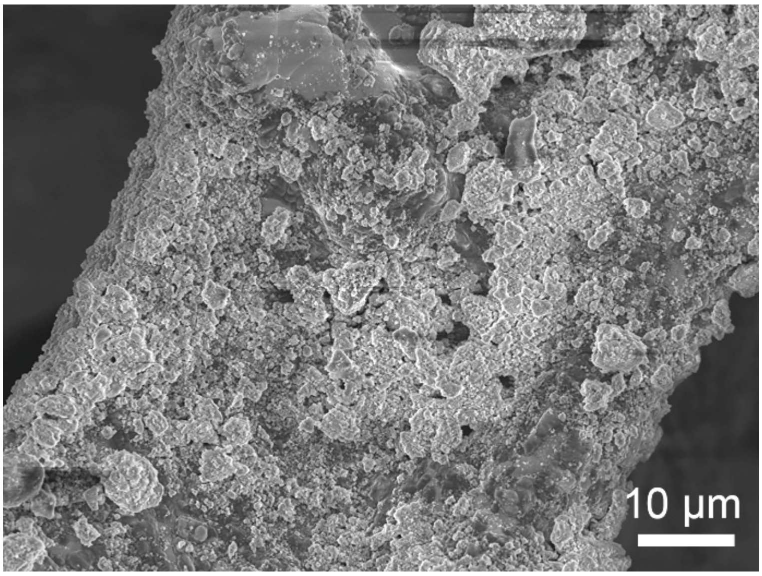

Figure S1. SEM image of PMo_{12}–$Fe(OH)_3$ precursor loaded on NF.

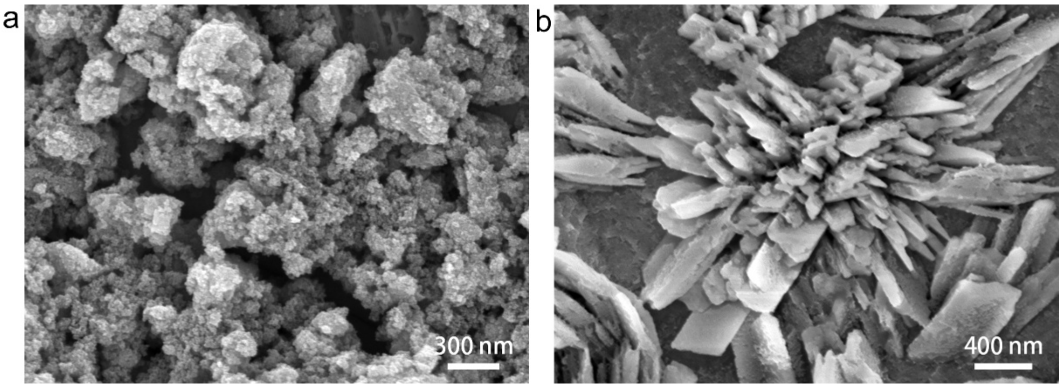

Figure S2. SEM images of (a) Fe_2O_3 and (b) MoO_3 samples lasered on NF.

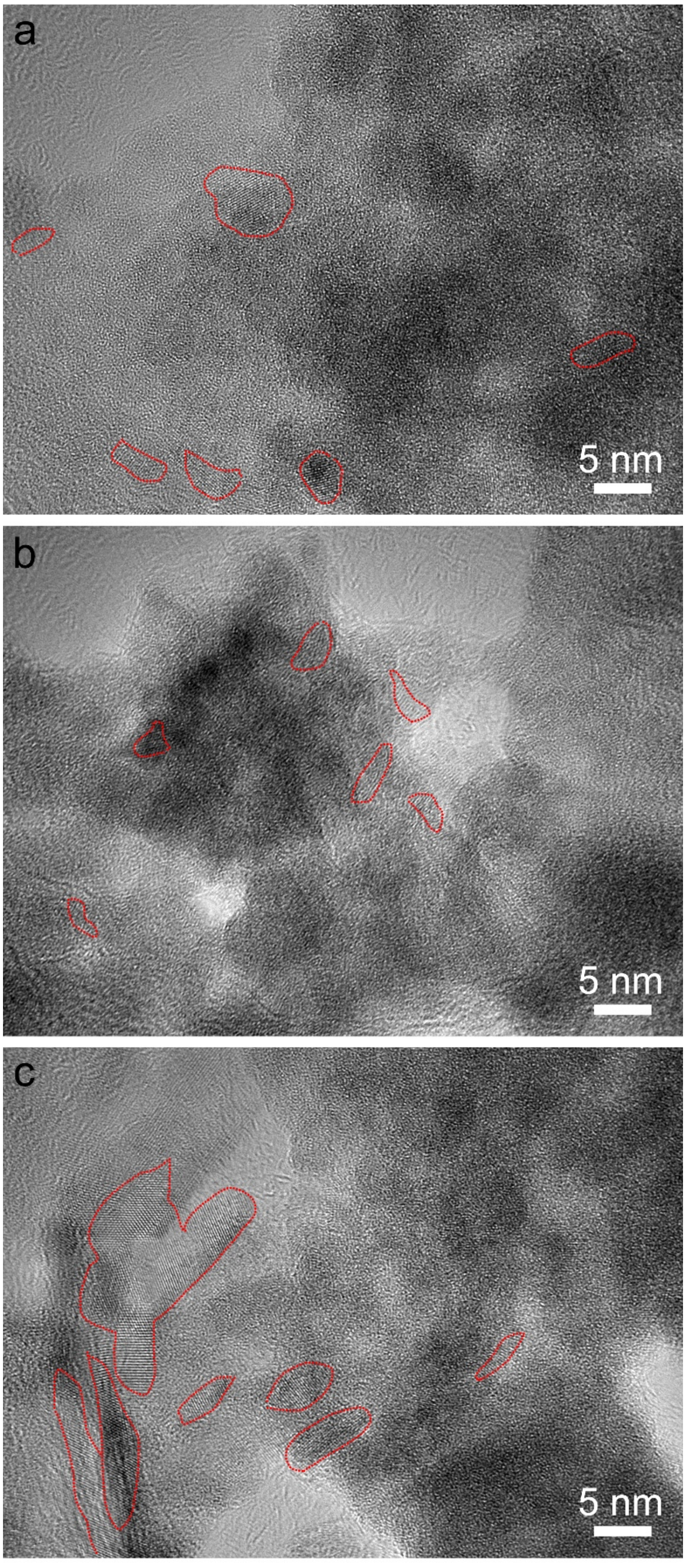

Figure S3. (a-c) HRTEM images of Fe_2O_3–MoO_3 heterostructure ultrasonicated from NF. Regions with distinct lattice fringes are marked by red dashed lines.

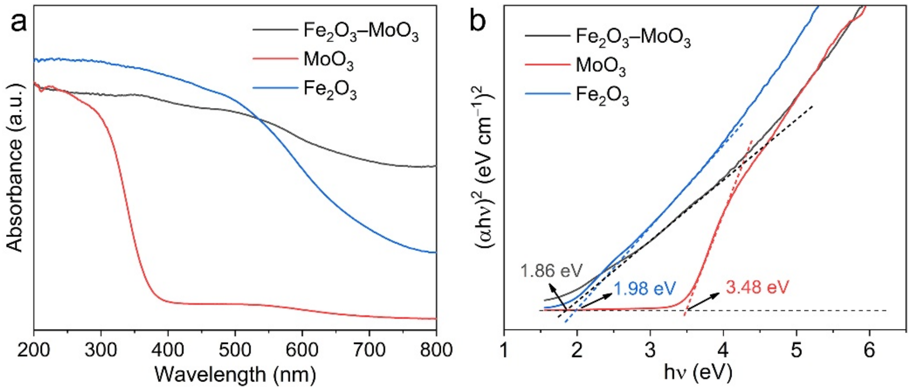

Figure S4. (a) UV-vis diffuse reflectance spectra and (b) Tauc plots of Fe_2O_3–MoO_3, Fe_2O_3, and MoO_3 samples peeled off from Ni foils.

To further prove the interfacial electron transfer from Fe to Mo, ultraviolet-visible diffuse reflectance spectroscopy (UV-Vis DRS) measurements were performed. Due to a low mass loading of Fe_2O_3–MoO_3 on NF, the valid spectral signals could not be obtained. Therefore, we prepared Fe_2O_3–MoO_3 and control samples on Ni foils and then peeled off for the subsequent UV-Vis DRS measurements.

Compared with the Fe_2O_3 and MoO_3 samples, the UV-Vis DRS of the Fe_2O_3–MoO_3 heterostructure shows a new characteristic absorption band due to the interfacial charge transfer. Tauc plots indicate that the band gap energies of Fe_2O_3–MoO_3, MoO_3, and Fe_2O_3 are fitted to be 1.86, 3.48, and 1.98 eV, respectively. The low band gap energy of the amorphous Fe_2O_3–MoO_3 heterostructure confirms the strong electronic interaction at the interface, thus modulating the electronic structure for the enhanced electrocatalytic activity for OER.

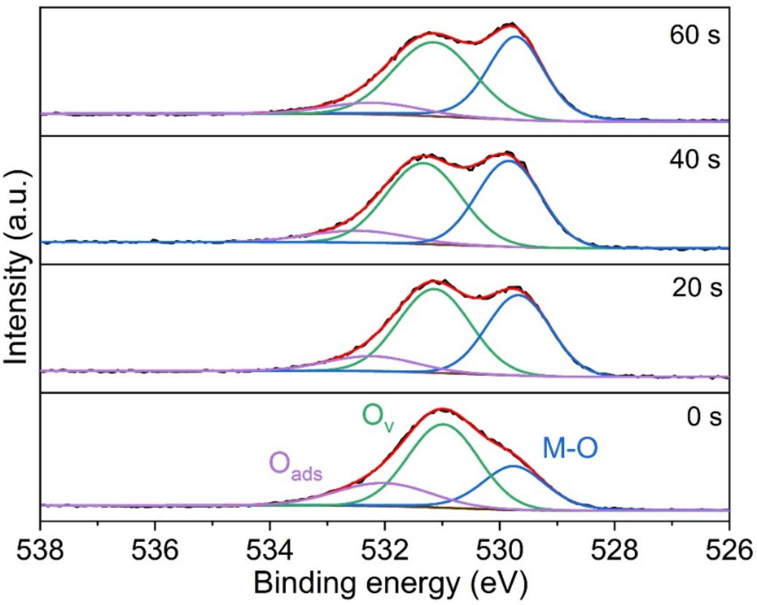

Figure S5. XPS depth profiling spectra of O 1s of Fe_2O_3–MoO_3 on NF.

As the profiling depth increased, the proportion of the adsorbed water (O_{ads}) peak at about 533.0 eV decreases, while the intensities of the O_v and M–O peaks increase significantly. This indicates that the oxygen vacancies are not induced by the surface environment and can serve as the stable active sites for OER. In addition, the above results further verify that the laser annealing strategy enables the construction of abundant defective structures and the formation of the oxide components.

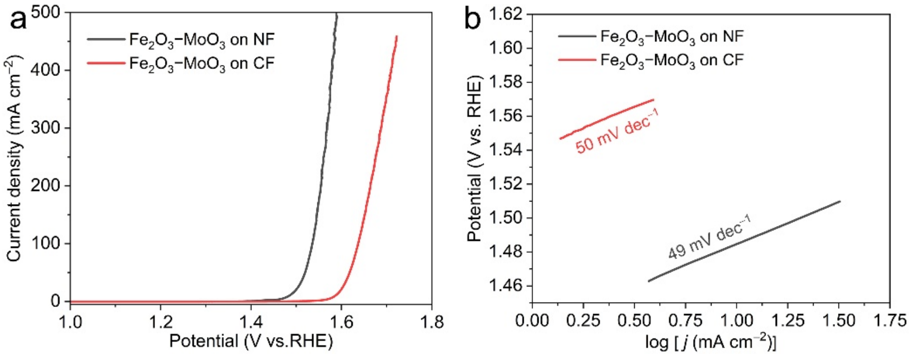

Figure S6. Electrocatalytic performance of Fe_2O_3–MoO_3 heterostructure loaded on CF and NF supports, respectively: (a) LSV curves, (b) Tafel plots.

The presence of Ni^{3+} species originated from the surface oxidation of the NF support contribute to the improved OER performance of the Fe_2O_3–MoO_3 heterostructure on NF to some extent. To prove the OER contribution of NF, we have measured the OER performance of the Fe_2O_3–MoO_3 heterostructure on the Cu foam (CF) substrate for comparison. The LSV curves show that Fe_2O_3–MoO_3 on CF has a larger overpotential of 410 mV at 100 mA cm^{-2} than that of the sample on NF (300 mV). The Tafel slope of Fe_2O_3–MoO_3 on CF is 50 mV dec^{-1}, which is also larger than the sample on NF (49 mV dec^{-1}). Therefore, the NF support plays a role for the enhancement of the OER performance.

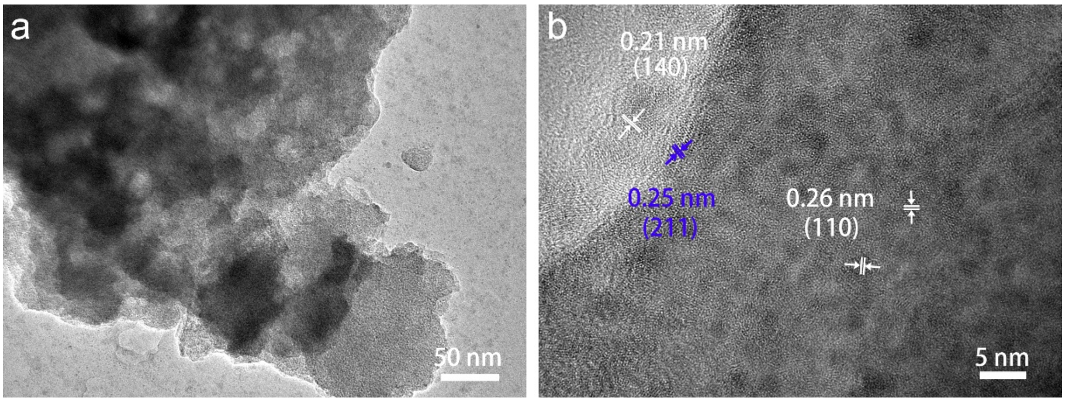

Figure S7. (a) TEM and (b) HRTEM images of Fe_2O_3–MoO_3 ultrasonicated from NF.

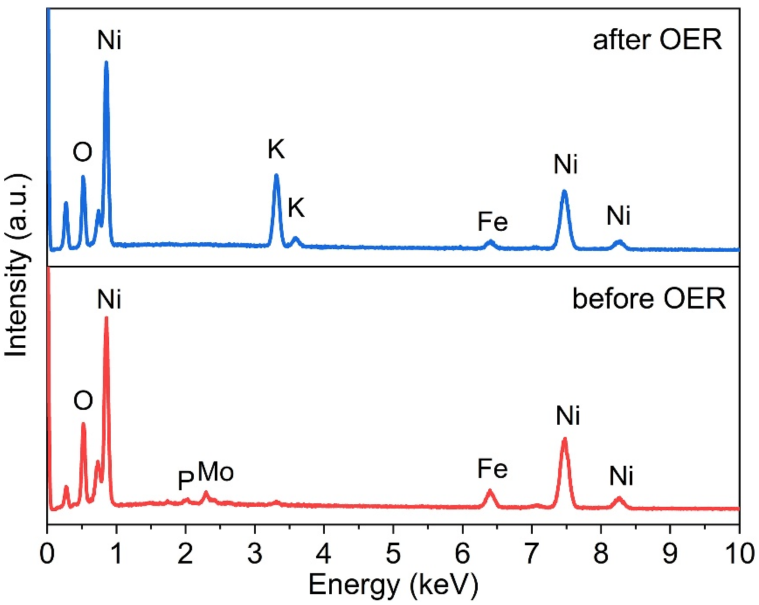

Figure S8. EDX spectra of Fe_2O_3–MoO_3 on NF measured before and after OER.

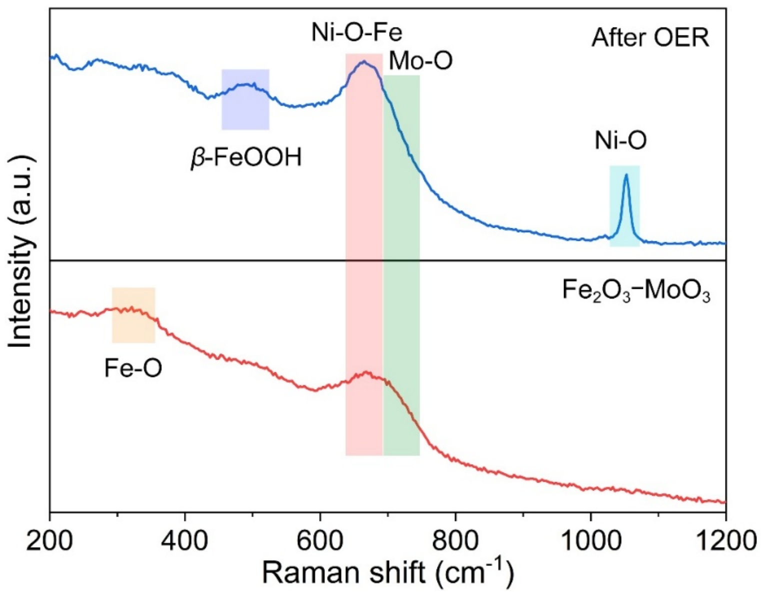

Figure S9. Raman spectra of Fe_2O_3–MoO_3 heterostructure on NF before and after OER.

The broad Raman peaks suggest the amorphous structures in the Fe_2O_3–MoO_3 catalyst. The Raman bands at about 670 and 730 cm^{-1} represent the characteristic Ni–O–Fe and Mo–O vibrations due to the Fe/Mo-based oxide components on NF.[1] The Raman band at 320 cm^{-1} assigns to the E_g mode of α-Fe_2O_3.[2] After OER, the Raman band at 500 cm^{-1} confirms the generation of new β-FeOOH phase, along with the appearance of the Ni–O band signal at 1050 cm^{-1} due to the oxidation of the NF support after OER.[3]

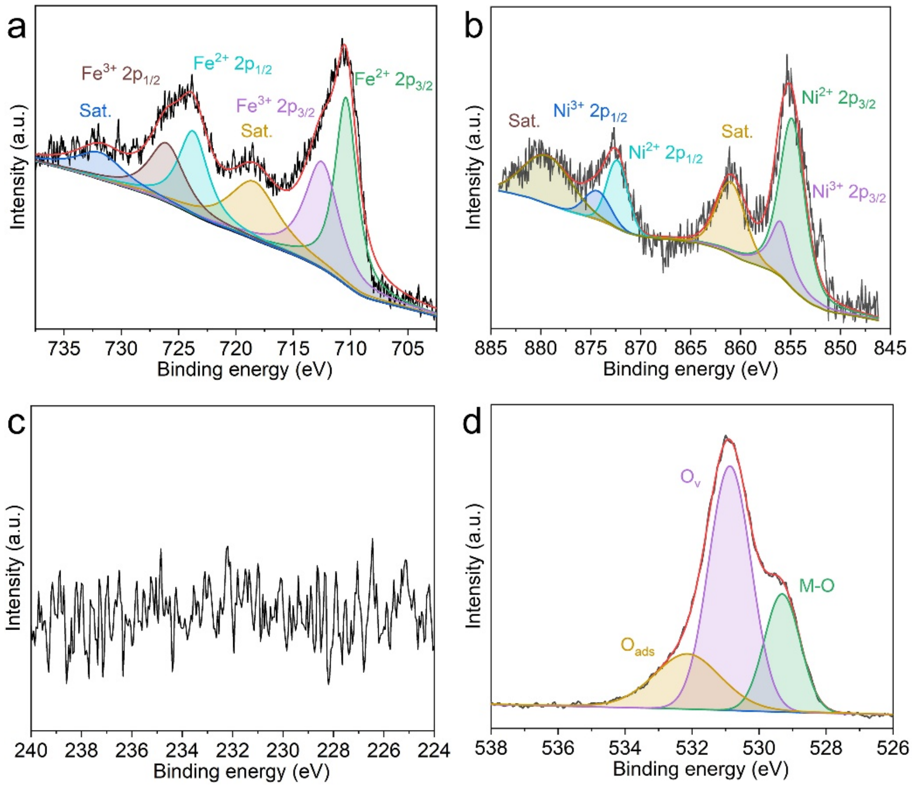

Figure S10. High-resolution XPS spectra of Fe_2O_3–MoO_3 on NF after OER: (a) Fe 2p, (b) Ni 2p, (c) Mo 3d, and (d) O 1s.

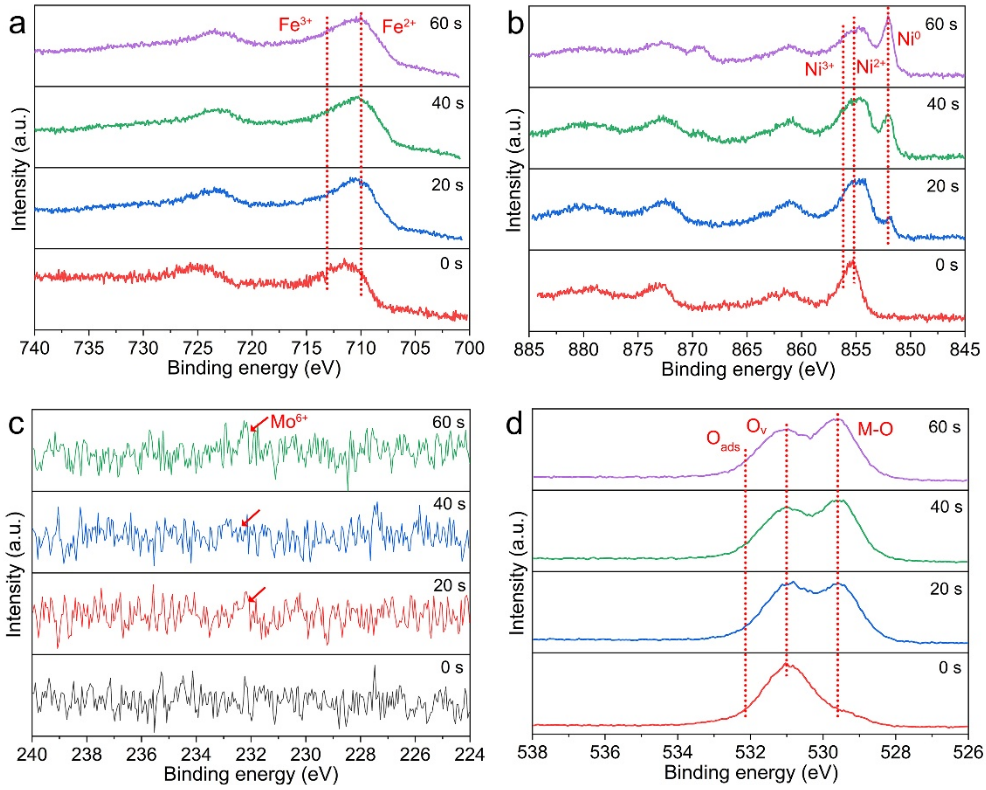

Figure S11. XPS depth profiling spectra of Fe_2O_3–MoO_3 on NF after OER: (a) Fe 2p, (b) Ni 2p, (c) Mo 3d, and (d) O 1s.

With increasing profiling depth, the peaks in the Fe $2p_{3/2}$ region show no obvious changes and can still be deconvoluted into the Fe^{3+} and Fe^{2+} peaks. In addition, slight negative shifts are observed for the Fe $2p_{3/2}$ peaks, revealing that the FeOOH species after OER is mainly formed on the surface while the Fe_2O_3 component remains in the bulk. The Ni 2p spectra show that the Ni^0 peaks derived from the NF substrate are observed as the profiling depth increases. The Mo 3d spectrum obtained at 0 s demonstrates no obvious Mo peaks due to the dissolution of the Mo species during the OER. As the profiling depth increases, the intensity of the Mo 3d peak at about 232.5 eV slightly increases, suggesting the residual Mo species existing in Fe_2O_3–MoO_3. The O 1s spectra show that the proportion of the peak of the M–O bond increases with the increasing profiling depth, confirming the retention of the metal oxides in the bulk. Meanwhile, the intensity of O_v exhibits no obvious changes, further verifying that the laser annealing treatment successfully constructs abundant oxygen vacancies.

Table S1. Comparison of Fe_2O_3–MoO_3 on NF and recently reported Fe-/Mo-based and POM-derived electrocatalysts for OER.

Electrocatalyst	Electrolyte	Substrate	η_{10} (mV)	Tafel slope (mV dec^{-1})	
Fe_2O_3–MoO_3	**1 M KOH**	**Ni foam**	**250**	**49**	**This work**
2D CuO nanosheet	1 M KOH	Stainless steel	350	59	4
$Co_{2.25}Fe_{0.75}O_4$	1 M KOH	Glassy carbon electrode	350	50	5
Fe_2O_3-N-CNHo$_x$550	1 M KOH	Carbon fiber paper	260	75.8	6
Li-α-MoO_3	1 M KOH	Carbon fiber paper	458	76	7
$MoO_3/Fe_2O_3/MoS_2$	1 M KOH	Ni foam	267	48.9	8
MoO_2@N/Mo–ReS_2	1 M KOH	Carbon cloth	249	63.7	9
NiMoNS	1 M NaOH	Ni foam	260	54.7	10
MoO_3/NiFe-LDH	1 M KOH	Ni foam	212	63.6	11
m-Fe/N-C@CNT	1 M KOH	Ni foam	338	104.9	12
P-MoO_3/FeCo LDH	1 M KOH	Ni foam	225	87.4	13
Ir/WO_x/rGO	1 M KOH	glassy carbon electrode	265	62	14
$CoMoO_4$ HTs	1 M KOH	Ni foam	210	80.3	15
Co_{SA}-$MoCeO_x$	0.5 M H_2SO_4	Ni foam	239	29	16

Table S2. Atomic percentage of corresponding elements of Fe, Ni, Mo, C, P, and O of Fe_2O_3–MoO_3 heterostructure on NF before and after OER measured by XPS.

Atomic %	Fe 3s	Ni 3s	P 2p	Mo 3d	C 1s	O 1s	Fe 2p	Ni 2p
Before OER	1.24	16.82	2.54	2.34	26.21	37.61	3.41	9.82
After OER	1.65	9.34	1.87	0.21	17.77	52.99	9.48	6.7

References

1 K. Dastafkan, S. Wang, C. Rong, Q. Meyer, Y. Li, Q. Zhang and C. Zhao, *Adv. Funct. Mater.*, 2022, **32**, 2107342.

2 Y. Liu, Q. He, Z. Wang, X. Jiao and Y. Zhang, *Microsc. Res. Tech.*, 2025, **88**, 154–162.

3 J. Hu, S. Li, J. Chu, S. Niu, J. Wang, Y. Du, Z. Li, X. Han and P. Xu, *ACS Catal.*, 2019, **9**, 10705–10711.

4 S. M. Pawar, B. S. Pawar, B. Hou, J. Kim, A. T. Aqueel Ahmed, H. S. Chavan, Y. Jo, S. Cho, A. I. Inamdar, J. L. Gunjakar, H. Kim, S. Cha and H. Im, *J. Mater. Chem. A*, 2017, **5**, 12747–12751.

5 S. Saddeler, G. Bendt, S. Salamon, F. T. Haase, J. Landers, J. Timoshenko, C. Rettenmaier, H. S. Jeon, A. Bergmann, H. Wende, B. Roldan Cuenya and S. Schulz, *J. Mater. Chem. A*, 2021, **9**, 25381–25390.

6 Y. Nan, Z. Zhang, Y. He, J. Wei and Y. Zhou, *Inorg. Chem.*, 2021, **60**, 16529–16537.

7 K.-H. Kim, D. Hong, M. G. Kim, W. Choi, T. Min, Y.-M. Kim and Y.-H. Choi, *ACS Mater. Lett.*, 2023, **5**, 1196–1201.

8 Z. Li, W. Tao, Y. Wang, X. Ye, Y. Chen, B. Han and L. Y. S. Lee, *J. Am. Chem. Soc.*, 2025, **147**, 24461–24472.

9 M. Singh, J. Park, H. Kim, G. Kim, D. Cha, D. R. Paudel, B.-H. Kim and S. Lee, *Small*, 2025, **21**, 2505906.

10 Y. Liu, P. Liu, Y.-L. Men, Y. Li, C. Peng, S. Xi and Y.-X. Pan, *ACS Appl. Mater. Interfaces*, 2021, **13**, 26064–26073.

11 H. Jiang, Y. Yu, X. Duan, P. Chen, S. Wang, X. Qiu, L. Ye and X. Tu, *Small*, 2024, **20**, 2307797.

12 R. Gan, Y. Song, C. Ma and J. Shi, *Appl. Catal. B-Environ.*, 2023, **327**, 122443.

13 C. Huang, J. Nie, Z. Xu, X. Zhang, J. Tang, B. Wang, J. Huang, C. Du and J. Chen, *Int. J. Hydrogen Energy*, 2021, **46**, 12992–13000.

14 B. Huang, Y. Ma, Z. Xiong, Z. Xiao, P. Wu, P. Jiang and M. Liang, *Energy Environ. Mater.*, 2021, **4**, 681–686.

15 Z. Zhang, J. Ran, E. Fan, S. Zhou, D.-F. Chai, W. Zhang, M. Zhao and G. Dong, *J. Alloys*

Compd., 2023, **968**, 172169.

16 J. Liu, T. Wang, Z. Lin, M. Liao, S. Liu, S. Wang, Z. Cai, H. Sun, Y. Shen, Y. Huang and Q. Li, *Energy Environ. Sci.*, 2024, **17**, 3088–3098.